Local potential and polarization screening on ferroelectric surfaces

Sergei V. Kalinin and Dawn A. Bonnell*
Department of Materials Science and Engineering, University of Pennsylvania, 3231 Walnut St. Philadelphia, Pennsylvania 19104

(Received 29 August 2000; published 13 March 2001)

Electrostatic force microscopy and scanning surface potential microscopy are applied to study force gradient and surface potential on $BaTiO_3(100)$ surface. Surface potential evolution during a ferroelectric/paraelectric phase transition and the potential distribution near moving domain walls allow the relationship between potential polarity and polarization orientation. Results indicate that polarization bound charge is completely screened on this surface and domain potential is reverse to that expected from domain polarity. Surface potential is attributed to the formation of double layer due to the complete screening of polarization charge. The absolute value of the measured potential difference between domains of opposite polarity suggests that surface adsorbates play a governing role in potential formation mechanism, though intrinsic screening by free carriers is not completely excluded.

DOI: 10.1103/PhysRevB.63.125411 PACS number(s): 77.80.Bh, 07.79.−v, 77.80.Dj, 73.30.+y

I. INTRODUCTION

Possible applications of ferroelectric materials in nonvolatile memories (FRAM),[1] microelectromechanical systems (MEMS),[2] microwave ceramics, positive temperature coefficient of resistance (PTCR) devices, sensors and actuators draw significant interest to these materials.[3–7] The operation of most of these devices relies heavily on the surface (FRAM and other thin-film devices) and interface (PTCR, varistors) properties of ferroelectrics materials. Details of the polarization and charge distribution in the surface/interface layers of ferroelectrics and their relationship to the physical properties of materials have been studied for more than four decades and are largely unresolved. Possible causes of surface layers include nonuniform vacancy distributions in the near-interface region, compensation of polarization-induced charges by band bending (intrinsic field effect) or adsorption (extrinsic field effect), and the existence of surface/interface states and corresponding Schottky depletion regions.[8–12] A closely related issue is the domain structure at surfaces and interfaces. These considerations have motivated a number of observations of ferroelectric materials with scanning probe based microscopies (SPM). Contact and intermittent mode atomic force microscopy, along with lateral force microscopy, have been widely used to characterize domain-related topographic features.[13–21] Direct information about local polarization, charge distribution, and electromechanical properties of surfaces can be obtained by such techniques as scanning surface potential microscopy (SSPM), electrostatic force microscopy (EFM),[22–27] and piezoresponse force microscopy (PFM).[28–32] However, the contrast formation mechanism in many variants of SPM is yet unclear due to the complexity of tip-surface interactions.

The present paper presents an approach for quantifying surface properties of ferroelectric materials from noncontact SPM measurements. Previous work treated the case of inhomogeneous surface potential in a linear dielectric material.[33] Here, tip-surface interactions exerted by screened and unscreened polarization bound charge are explicitly included. A mathematical model based on a simplified image charge distribution in the tip is used to relate SPM measurements to surface properties. Observations of the ferroelectric phase transition on $BaTiO_3(100)$ surface by variable temperature SSPM and piezoresponse force microscopy and the potential distribution in the vicinity of a moving domain wall are used to establish the relationship between local polarization variations and effective surface potential. The properties of an electric double layer and the presence of uncompensated Coulombic charge have been extracted from EFM and SSPM data.

II. THEORETICAL DEVELOPMENT

Both EFM and SSPM are based on the dual pass scheme. The grounded tip first acquires the surface topography using standard intermittent contact atomic force microscopy (AFM). Electrostatic data are collected above the surface. In EFM, the cantilever is driven mechanically and the electrostatic force F between the dc biased conductive tip and the surface results in a change of the cantilever resonant frequency that is proportional to the force gradient[34]

$$\Delta\omega = \frac{\omega_0}{2k}\frac{dF(z)}{dz}, \qquad (1)$$

where k is the spring constant and ω_0 is the resonant frequency of the cantilever. Resonance is maintained by adjusting the driving frequency ω_p and the frequency shift $\Delta\omega = \omega_p - \omega_0$ is collected as the EFM image.

In SSPM the cantilever is not driven mechanically; rather, the tip is biased directly by $V_{tip} = V_{dc} + V_{ac}\cos(\omega t)$, where V_{ac} is referred to as the driving voltage. The capacitive force $F_{cap}(z)$ between the tip and a surface at potential V_s is

$$F_{cap}(z) = \frac{1}{2}(V_{tip} - V_s)^2 \frac{\partial C(z)}{\partial z}, \qquad (2)$$

where $C(z)$ is the tip-surface capacitance dependent on tip geometry, surface topography and tip-surface separation z. The first harmonic of the force is

$$F_{1\omega}^{cap}(z) = \frac{\partial C(z)}{\partial z}(V_{dc} - V_s)V_{ac} \qquad (3)$$

 ©2001 The American Physical Society

and feedback is used to nullify this term by adjusting the constant component of the tip bias V_{dc}. This condition is met when V_{dc} is equal to surface potential and thus, mapping the nulling potential V_{dc} yields a surface potential map. A closely related imaging technique is piezoresponse force microscopy (PFM). In PFM the tip is brought into contact with the surface and the piezoelectric response of the surface is detected as a first harmonic component of bias-induced tip deflection $d=d_0+A\cos(\omega t+\varphi)$. The phase φ yields information on the polarization direction below the tip. For a polarization vector pointing downwards (i.e., c^- domains), the application of a positive tip bias results in the expansion of the sample and bias-induced surface oscillations are in phase with tip voltage $\varphi=0$. For polarization pointing upwards (i.e., c^+ domains) $\varphi=180°$. The amplitude A defines the local piezoresponse and depends on the geometry of the system (thin film[35] vs bulk crystal or ceramics). The numerical value of A under ideal imaging conditions (perfect contact between the tip and the surface, no viscous damping) is determined by combination of a electroelastic constants of material[36–40] and tip properties. A number of approximate treatments of piezoresponse contrast in thin films have also been reported.[41–44] It is generally assumed that SSPM provides quantitative information on local potential related to polarization, the screening mechanism, and the presence of intrinsic surface states and adsorbates. PFM provides information on polarization through local piezoresponse; however, image contrast in PFM may include contributions due to Maxwell stresses,[45] polarization switching below the tip, etc. Despite the difficulties related to the quantification of PFM it is readily used qualitatively to determine the out-of-plane component of local polarization, i.e., domain orientation. Imaging the in-plane component of local polarization has also been reported.[32,46]

Quantification of surface properties of a ferroelectric material from EFM and SSPM data requires the solution of several independent problems. First, these techniques are ultimately sensitive to the force gradient (EFM) or the force (SSPM) between the tip and the surface. The origins of electrostatic tip-surface interaction and corresponding models are discussed in Sec. II A. Second, the measurements are performed above the surface rather than through the depth of surface layer so an extrapolation is necessary. A simplified model of potential and charge distribution on a ferroelectric surface is considered in Sec. II B. EFM and SSPM of ferroelectric surfaces are considered in Secs. II C and II D, respectively.

A. Tip-surface interaction

Quantification of the electrostatic properties of surfaces by EFM and SSPM is impossible without the detailed analysis of capacitive tip-surface interactions as shown in Ref. 33. In the case of ferroelectric materials the inhomogeneous distribution of ferroelectric domains requires that the cantilever contribution must also be included. Image charge models such as the line and point charge models[47–49] can be used to construct approximate solutions for nonuniform systems at intermediate and small tip-surface separations. Using the line charge model the force and force gradient are

$$F_{cap}=\frac{\lambda^2}{4\pi\varepsilon_0}\ln\left(\frac{L}{4h}\right) \tag{4a}$$

and

$$\frac{dF_{cap}}{dz}=\frac{\lambda^2}{4\pi\varepsilon_0}\frac{1}{h}, \tag{4b}$$

where h is the separation between the tip apex and surface and L is the effective tip size. The line charge density λ is

$$\lambda=\frac{4\pi\varepsilon_0 V}{\beta}, \tag{5}$$

where β depends on the equipotential surface geometry.

Capacitive tip-surface interactions for a tip shape including tip bulk and rounded tip apex results in a total force and force gradient acting on the tip

$$F_{cap}=V^2\left[\frac{\gamma}{z}+\eta\ln\left(\frac{D}{z}\right)\right] \tag{6a}$$

and

$$\frac{dF_{cap}}{dz}=V^2\left(-\frac{\gamma}{z^2}+\frac{\eta}{z}\right) \tag{6b}$$

where γ, η and D are tip-shape dependent parameters which are found experimentally from force or force-gradient–distance dependencies.

The cantilever contribution to total force and force gradient can be approximated by a plane-plane capacitor in which

$$F_{cap}=\frac{\varepsilon_0 V^2}{2}\frac{S}{(z+L)^2} \tag{7a}$$

and

$$\frac{dF_{cap}}{dz}=-\varepsilon_0 V^2\frac{S}{(z+L)^3}, \tag{7b}$$

where S is the effective cantilever area and L is the tip length. For a typical metal coated tip used in the EFM/SSPM measurements with $R\approx 30\,\text{nm}$, $\theta=17°$, $L\approx 10\,\mu\text{m}$ and $S\approx 2\times 10^3\,\mu\text{m}^2$, the contributions of the tip apex, tip bulk and cantilever to the overall force and force gradient are shown in Fig. 1. As seen from Fig. 1(a), for intermediate and large tip-surface separation the cantilever provides the largest contribution to electrostatic force. The major contribution to force gradient is due to the tip bulk, the cantilever providing a distance-independent offset. A realistic cantilever configuration (i.e., tilted with respect to the surface) results in a smaller force and force gradient; nevertheless, the estimates presented here are still valid.

B. Charge and potential of ferroelectric surfaces

In quantification of electrostatic SPM on ferroelectric materials the vast majority of authors assume that a ferroelectric surface is characterized by an unscreened polarization charge density $\sigma=\mathbf{P}\cdot\mathbf{n}$, where $\mathbf{P}$ is the polarization vector and $\mathbf{n}$ is the unit normal to the surface.[50–52] It is well known, how-

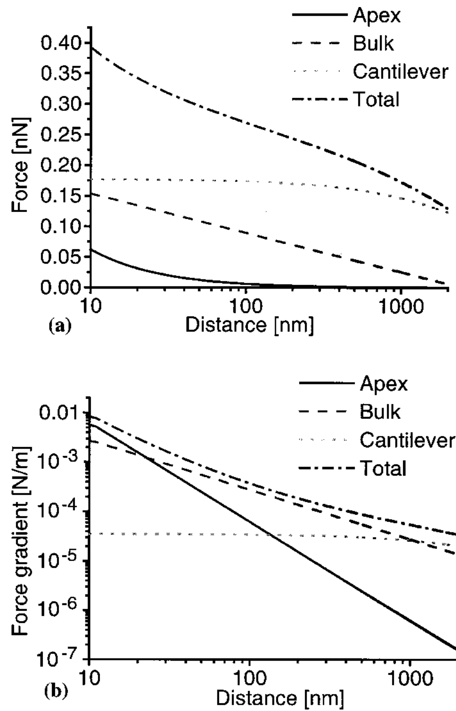

FIG. 1. Relative contributions of tip apex, tip bulk and the cantilever to the total electrostatic force (a) and force gradient (b) for tip parameters defined in text. Force gradient is proportional to the frequency shift measured in the EFM.

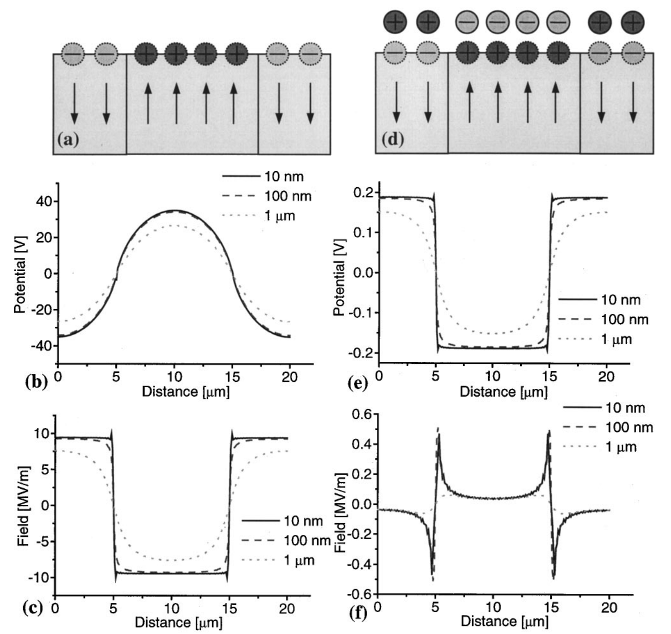

FIG. 2. Potential (a), (c) and the field (b), (d) in the vicinity of ferroelectric surface for unscreened (a), (b) and completely screened (c), (d) cases. Distances indicate the separation from the surface. Note that uniform and domain size independent image contrast can be attributed either to the electric field for the unscreened surface or potential for the completely screened surface.

ever, that polarization is always screened on ferroelectric surfaces.[53] The screening can be due to adsorbates and/or surface states or free charges with associated depletion or accumulation layers. In the latter case an additional constraint is that the electric field in the surface layer cannot exceed the coercive field.[54]

To quantitatively address electrostatic properties of ferroelectric surfaces the surface layer is represented with polarization charge $\sigma_{\mathrm{pol}}=\mathbf{P}\cdot\mathbf{n}$ and screening charge equivalent to surface charge density σ_s of the opposite polarity. The following cases can be distinguished: (1) completely unscreened $\sigma_s=0$, (2) partially screened $\sigma_{\mathrm{pol}}>-\sigma_s$, (3) completely screened $\sigma_{\mathrm{pol}}=-\sigma_s$, and (4) overscreened $\sigma_{\mathrm{pol}}<-\sigma_s$. A completely unscreened surface is extremely unfavorable from an energetic point of view. An overscreened surface is likely to occur during bias-induced domain switching and indeed has been observed.[55,56] Partially or completely screened surfaces are likely to be the usual state of ferroelectric surfaces in air. The charge distribution on a ferroelectric surface is described in terms of a double layer of width h, dipole moment density $h\cdot\min[\sigma_{\mathrm{pol}},\sigma_s]$ and an uncompensated charge component, $\delta\sigma=\sigma_{\mathrm{pol}}-\sigma_s$. Depending on the relative spatial localization of the polarization and screening charges, surface potential in the completely screened case can have the same sign as σ_{pol}, or be of the opposite sign.

Usually noncontact measurements are performed at tip-surface separations of 10–100 nm, which is much smaller then typical domain sizes ($\sim$1–10 μm). For completely screened and unscreened surfaces the typical values of potential and field are shown in Fig. 2 (the Appendix). For the partially screened surfaces the potential and the field are a linear superposition of profiles for completely screened and unscreened surfaces. Simple arguments predict that surface potential above the unscreened surfaces and electric field above the completely screened surfaces scale linearly and reciprocally with domain size, while electric field over the unscreened surfaces and potential over the screened surfaces are virtually domain size independent.

The detailed analysis of tip-surface interactions in EFM and SSPM of ferroelectric surfaces is presented in the next two sections. However, as shown in Fig. 2, the experimentally observed uniform image contrast within the domain can be attributed either to the potential variation above the surface and corresponding change of the capacitive interaction [Eqs. (2) and (3)], or the variation in the surface charge density and normal electric field that results in additional Coulombic interaction between the tip and the surface. Hence image contrast alone is insufficient to distinguish these contributions and detailed analysis of force gradient-distance (EFM) and force-distance (SSPM) data is required.

C. EFM imaging of ferroelectric surfaces

As discussed in Sec. II A, the force gradient acting on the probe at intermediate tip-surface separations is governed by tip bulk and cantilever contributions. Assuming that domain size is comparable or larger than the tip size (which is usually true), but much smaller then the cantilever size, the tip interacts with a single domain, and the cantilever detects the average surface potential. In the following discussion the po-

larization charges are assumed to be almost completely screened by surface adsorbates and/or free carriers, equivalent to the presence of a double layer, characterized by potential V_s. The contribution of a Coulombic interaction F_{coul} related to the uncompensated surface charge density $\delta\sigma$ is omitted for simplicity but can be easily incorporated.

The capacitive electrostatic force between the tip and the surface is

$$F(z)=(V_{\mathrm{tip}}-V_s)^2F_t(z)+(V_{\mathrm{tip}}-V_{\mathrm{av}})^2F_c(z), \tag{8}$$

where $F_t(z)$ is tip contribution and $F_c(z)$ is cantilever contribution.

Force gradient can be derived from Eq. (8) and after the grouping

$$F'(z)=V_{\mathrm{tip}}^2(F_t'+F_c')+V_{\mathrm{tip}}(-2V_sF_t'-2V_{\mathrm{av}}F_c')+V_s^2F_t'+V_{\mathrm{av}}^2F_c'. \tag{9}$$

The average force gradient determined experimentally as the average of all image points is

$$F_{\mathrm{av}}'(z)=V_{\mathrm{tip}}^2(F_t'+F_c')-2V_{\mathrm{tip}}V_{\mathrm{av}}(F_t'+F_c')+V_{\mathrm{av}}^2(F_t'+F_c') \tag{10}$$

or

$$F_{\mathrm{av}}'(z)=A_2V_{\mathrm{tip}}^2+A_1V_{\mathrm{tip}}+A_0 \tag{11}$$

provided that the image size is large compared to the domain size. It should be noted here that the frequency shift proportional to the force gradient experimentally measured in EFM often has an additive constant due to the slow drift of the oscillation characteristics of the cantilever, but quadratic and linear coefficients in tip bias can be easily extracted.

The force gradient difference between domains of different polarities with surface potentials V_1 and V_2 is

$$F_d'(z)=-2V_{\mathrm{tip}}(V_1-V_2)F_t'+(V_1^2-V_2^2)F_t' \tag{12}$$

or

$$F_d'(z)=B_1V_{\mathrm{tip}}+B_0. \tag{13}$$

Provided that the experimentally determined average force gradient and the difference in force gradients above domains with different polarity are quadratic and linear in voltage, respectively, the constants A_2, A_1 and B_1, B_0 can be extracted. Our previous estimates (Fig. 1) suggest that F_c' can be neglected compared to F_t' for intermediate tip-surface separations. In this case, in the absence of a Coulombic contribution from unscreened charges the coefficients in Eqs. (11), (13) yield the following universal ratios:

$$\frac{B_1}{A_2}=-2(V_1-V_2),\quad \frac{B_0}{B_1}=\frac{V_1+V_2}{-2},\quad \frac{A_1}{A_2}=-2V_{\mathrm{av}}. \tag{14}$$

Noteworthy is that these ratios are independent of the probe properties and are distance independent. Conversely, if these ratios are distance independent, then the observed contrast between domains of different polarity can be attributed to the double layer contrast without a free charge contribution, since the distance dependencies of the two are different. By fitting the distance dependence of A_2 and B_1 to Eq. (6a) the relative contributions of the tip apex and the tip bulk to the overall force gradient can be estimated.

The Coulombic contribution to the tip-surface force and force gradient related to the unscreened charge can be estimated using a line charge model similarly to Ref. 32. The total force between the biased tip and the surface can be written as

$$F(z)=\frac{dC(z)}{dt}\Delta V^2+\int\frac{\partial\varphi_{\mathrm{sc}}}{\partial\mathbf{n}}(\sigma_{\mathrm{tip}}+\sigma_{\mathrm{ind}})d\mathbf{S}_{\mathrm{tip}}, \tag{15}$$

where the first term is the capacitive force $F_{\mathrm{cap}}(z)$ discussed in Sec. II A and the second term is a contribution due to the Coulombic interaction of uncompensated charges with the metallic tip $F_{\mathrm{coul}}(z)$. σ_{tip} is surface charge density of the tip without uncompensated charges, σ_{ind} is the image charge density induced by uncompensated charge, and $\mathbf{n}$ is the normal vector to the tip surface. Assuming that the second term in Eq. (15) is much smaller than the first, $\sigma_{\mathrm{ind}}\ll\sigma_{\mathrm{tip}}$, the second term in Eq. (15) becomes

$$\int\frac{\partial\varphi_{\mathrm{sc}}}{\partial\mathbf{n}}\sigma_{\mathrm{tip}}d\mathbf{S}_{\mathrm{tip}}=\int_d^{L+d}\lambda_{\mathrm{tip}}\varphi_{\mathrm{sc}}'dz=\lambda_{\mathrm{tip}}\varphi_{\mathrm{sc}}(d) \tag{16}$$

since $\varphi_{\mathrm{sc}}(z)$ rapidly decays with tip-surface separation. (The decay length for electric field is in this case comparable with characteristic domain size. For uniformly charged surfaces this assumption is no longer valid; however, the electric field can be assumed to be uniform in this case and the Coulombic force is then $F_{\mathrm{coul}}=\lambda LE_n$, hence the SPM contrast for Coulombic and capacitive interactions is similar.) Equation (16) implies that for a dominant Coulombic interaction tip-surface force is proportional to potential, while force gradient is proportional to electrostatic field. Hence domain contrast in force sensitive (SSPM) and force gradient sensitive (EFM) SPMs can be expected to differ, unlike the completely screened scenario in which EFM and SSPM profiles are similar.

D. SSPM imaging of ferroelectric surface

In order to quantify the SSPM contrast of ferroelectric surfaces both the cantilever contribution and the nonideality of feedback loop must be taken into account.[33,57] The first harmonic of the electrostatic force between the tip and a surface with complete screening is

$$F_{1\omega}(z)=V_{\mathrm{ac}}(V_{\mathrm{dc}}-V_s)F_t+V_{\mathrm{ac}}(V_{\mathrm{dc}}-V_{\mathrm{av}})F_c. \tag{17}$$

The operation of SSPM implies that

$$V_{\mathrm{dc}}=\frac{V_sF_t+V_{\mathrm{av}}F_c}{F_t+F_c}+\frac{\delta}{V_{\mathrm{ac}}(F_t+F_c)}, \tag{18}$$

where δ is constant dependent on feedback loop parameters. Similar to EFM image analysis, the average image potential

V_{dc}^{av} and the potential difference between domains of different polarity ΔV_{dc} can be defined as

$$V_{dc}^{av}=V_{av}+\frac{\delta}{V_{ac}(F_t+F_c)} \tag{19}$$

and

$$\Delta V_{dc}=(V_1-V_2)\frac{F_t}{F_t+F_c}. \tag{20}$$

If Eqs. (19) and (20) hold, the domain potential difference is independent of feedback operation. Taking expressions for the distance dependence of tip-surface forces [Eq. (4)] and cantilever-surface forces [Eq. (7)] and also taking into account that the cantilever contribution to the force dominates as shown on Fig. 1a, the measured domain potential contrast ΔV_{dc} is

$$\Delta V_{dc}\approx(V_1-V_2)\frac{F_t}{F_c}\approx(V_1-V_2)\frac{4\pi S}{L^2\beta^2}[\ln(L/4)-\ln(z)]. \tag{21}$$

Thus, experimentally measured potential differences between domains decay logarithmically with tip-surface separation. Figure 1(a) suggests that saturation occurs only for very small tip-surface separations, when the contribution of the tip apex to the force is dominant. In this case, however, the tip-induced field is very large and can induce polarization switching or screening charge redistribution below the tip. Hence EFM provides the true values of domain potential through universal ratios defined in Eq. (14) obtained by multiple scans at different tip biases, while SSPM, though being experimentally simpler, is unable to provide the correct value of domain potential difference.

III. EXPERIMENTAL PROCEDURES

The AFM and SSPM measurements were performed on a commercial instrument (Digital Instruments Dimension 3000 NS-III). Both conventional silicon tips ($l\approx125\,\mu$m, resonant frequency ~270 kHz) and metal coated tips ($l\approx225\,\mu$m resonant frequency ~60 kHz, $k\approx1-5$ N/m) were used. The lift height for the interleave scans in the SSPM was usually 100 nm. The scan rate varied from 0.2 Hz for large scans (~60 μm) to 1 Hz for smaller scans (~10 μm). Our studies indicated that surface potential observed by SSPM saturates at driving voltage ~1–2 V for lift heights used and thus driving voltage V_{ac} in the interleave scan was taken to be 5 V. To perform piezoresponse measurements, the AFM was additionally equipped with a function generator and lock-in amplifier (DS340, SRS 830, Stanford Research Systems). W_2C coated tips ($l\approx125\,\mu$m, resonant frequency ~350 kHz) (Silicon MDT NSCS 12 W_2C) were used for these measurements. These tips can also be used for SSPM measurements, however, due to the large spring constant ($k\approx40$ N/m) the noise level in EFM is unacceptably high.

Topographical images were processed by line flattening.[58] SSPM images were processed only by constant background substraction. Force gradient and potential profiles were obtained by averaging the flattened EFM and unprocessed SSPM images along the slow scan axis. A generic feature of SSPM is fewer imaging artifacts due to topography. Characteristic oscillation amplitude during potential detection is ~1 nm, therefore, for flat surfaces imaging is possible at very small tip-surface separation. In order to obtain a quantitative description of the EFM and SSPM measurements with a sharp tip and a blunted tip were compared. Usually 5–7 images were used to extract average and domain frequency shifts and force gradients.

Variable temperature measurements were performed on a home-built heating stage. During measurements, the temperature was increased in steps of ~10 °C and the system was kept at the selected temperature for ~0.5 h in order to achieve thermal equilibrium. The cantilever was retuned at each step in order to stay in the vicinity of the resonance frequency. Thermal drift was corrected by adjusting lateral offsets to position domain-unrelated topographical features. The lateral displacements of the tip with respect to the surface were usually 2–3 μm per 10 °C, except in the vicinity of the Curie temperature, where the ferroelectric phase transition was accompanied by significant (~10 μm) displacements.

A barium titanate (100) single crystal ($5\times5\times1$ mm, $T_c=130\,°$C, Superconductive Components, Inc.) was used in which the roughness of the (100) face did not exceed 15 Å. Prior to analysis the crystal was repeatedly washed in acetone and deionized water. In order to obtain a reproducible well-developed domain structure the crystal was heated above the T_c, kept at 140 °C for ~0.5 h and cooled down on a metallic surface.

IV. RESULTS AND DISCUSSION

Reconstruction of domain structure from the combination of AFM, SSPM and PFM is considered in Sec. IV A. The relationship between surface polarization and surface potential based on variable temperature measurement, domain wall motion and piezoresponse imaging is discussed in Sec. IV B. Bias and distance dependencies of EFM and SSPM images are quantified in Secs. IV C and IV D, respectively. Finally, the structure of surface layer on $BaTiO_3(100)$ is discussed in Sec. IV E.

A. Domain structure reconstruction

The surface domain structure of a ferroelectric surface can, in some cases, be unambiguously determined by SPM. Tetragonal symmetry of $BaTiO_3$ unit cell results in characteristic surface corrugations at 90° a-c domain walls. The corrugation angle is $\theta=\pi/2-2\arctan(a/c)$, where a and c are the parameters of the tetragonal unit cell. Complementary information on surface potential or polarization direction obtained by noncontact (SSPM, EFM) or contact (PFM) SPM allows the reconstruction of the surface domain structure.

The central part of the crystal is formed by large lamellar domains oriented at 45° to the edges of the crystal. The absence of significant topographic and potential variations allows this domain structure to be ascribed to $a1$-$a2$ domain

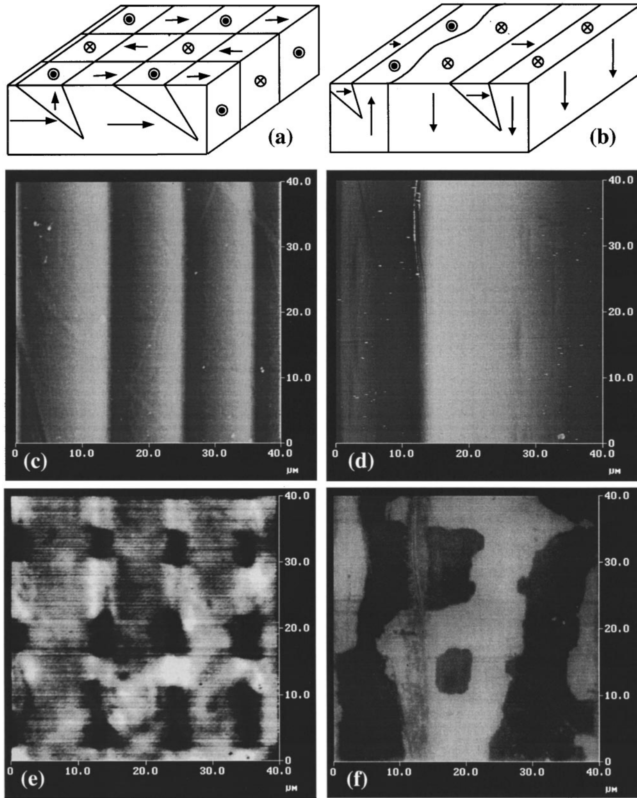

FIG. 3. Schematic diagrams of domain structure (a), (b), surface topography (c), (d) and surface potential (e), (f) in *a*-domain region with *c*-domain wedges (a), (c), (e) and in *c*-domain region with *a*-domain wedges (b), (d), (f). Scale is 50 nm [(c), (d)], 0.2 V [(e), (f)].

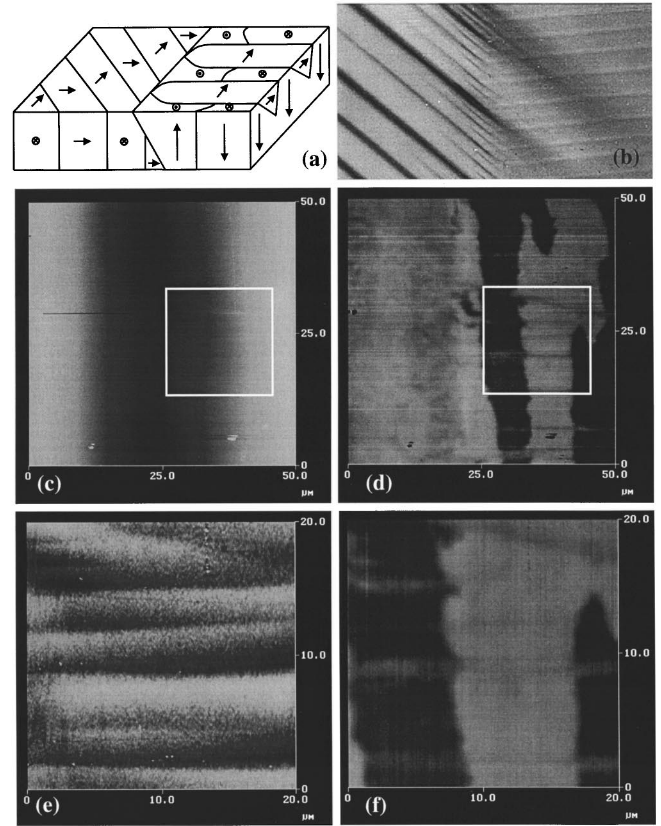

FIG. 4. Domain structure reconstruction (a), polarized light optical micrograph (b), surface topography (c), (e) and surface potential (d), (f) in the region with complex domain arrangement. Scale is 100 nm (c), 10 nm (e), 0.2 V [(d), (f)].

arrangements. Close to the edge of the crystal regions with a-c orientation are present. If the size of the c domains is relatively small, then 180° walls perpendicular to 90° domain boundaries between a and c domains [Figs. 3(a),(c),(e)] are formed. Similar domain arrangements are reported elsewhere.[59] This domain pattern can be ascribed to c-domain wedges in the crystal with dominating a-domain structure. The formation of 180° walls within the wedge minimizes the depolarization energy. If c-domain regions are large [Figs. 3(b),(d),(f)], irregular 180° walls separating c^+-c^- domains exist. These walls are continuous through a-domain regions, indicating the presence of a wedge domains in preferentially c-domain material [Figs. 3(b),(d),(f)]. More complex domain structures also occur. Figure 4 shows the boundary between regions with $a1$-$a2$ (left side) and c^+-c^- (right side) domain arrangements. The optical micrograph clearly indicates the presence of $a1$-$a2$ boundaries (left). Minor lines (right) can be observed only for small focus depths indicating a near-surface character. Large scale AFM imaging indicates that large surface corrugation [Fig. 4(c)] is associated with the presence of 90° domain wall. The surface potential indicates that the left region of the image is not associated with significant potential variations, while clear c^+-c^- domain regions are present on the right side. Noteworthy is that small horizontal potential features are also observed on the SSPM image. At higher resolution [Figs. 4(e), (f)] surface corrugations corresponding to the 90° domain walls are clearly seen [note the difference in vertical scales between Figs. 4(c) and (e)]. The surface potential image from the same region [Fig. 4(f)] shows both potential features corresponding to surface a-c domain and bulk c^+-c^- domain arrangements. This domain structure probably relieves the strain in the near-surface layer associated with macroscopic 90° domain wall between with $a1$-$a2$ and c^+-c^- domain regions.

Surface topography, surface potential (SSPM) and force gradient (EFM) images of a similar region are compared in Fig. 5. Note that for positive tip bias [Fig. 5(c)] the EFM image is similar to the SSPM image. For negative tip bias the EFM image is inverted, as expected. For zero tip bias the EFM image has the same sign as for a negatively biased tip, indicative of positive average surface potential [Fig. 5(d)].

B. Domain polarity

Polarization screening on ferroelectric surfaces can be determined from variable temperature measurements of surface properties. Above the Curie temperature of the ferroelectric phase transition spontaneous polarization disappears as evidenced by the disappearance of surface corrugations above T_c as shown in Fig. 6. This is also confirmed by variable temperature piezoresponse force microscopy.[60] Simultaneous

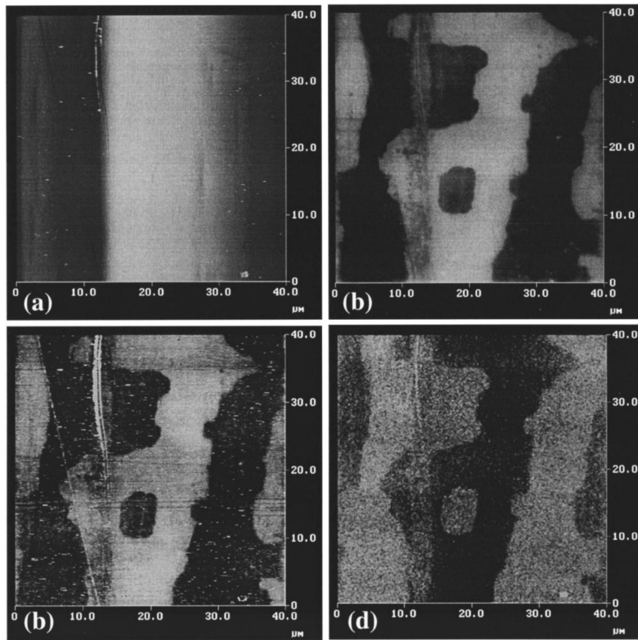

FIG. 5. Surface topography (a), surface potential (b) and EFM images of $BaTiO_3$ (100) surface at tip bias of 5 V (c) and 0 V (d).

SSPM indicates a spurious increase in surface potential amplitudes.[61,62] This effect is ascribed to the fact that screening charges are uncompensated after lattice polarization disappears above T_c. Consistent with this is that the sign of the potential features remains the same after the transition (Fig. 6). This implies that the sign of domain related potential features is governed by the screening charges and is opposite to that expected from polarization orientation. Specifically, c^+ domains are negative and c^- domains are positive on SSPM image. Further evidence supporting this model is provided by the phenomenon of temperature-induced potential inversion reported elsewhere.[63]

The relationship between polarization orientation and surface potential can also be established from the observation of domain wall motion. Shown in Fig. 7 are SSPM images of a c^+-c^- domain structure obtained at 12 h intervals. The shrinking of negative domains results in the formation of a dark rim in the direction of domain wall motion. Formation of the rim is ascribed to the slow relaxation of screening charges after the displacement of the domain wall. Simple considerations [Figs. 7(c),(f)] imply that a negative rim in the direction of wall motion is possible only if domain related potential features are determined by the screening charges. Formation of positive and negative rims during 90° a-c^- and a-c^+ domain wall motion was also observed.

The relationship between local polarization orientation and surface potential can also be established by comparison of SSPM and PFM imaging from the same region. Piezoresponse images of a $BaTiO_3$(100) surface are compared to SSPM images from the same region in Fig. 8. It can be seen that the signs of piezoresponse and surface potential images are the same, i.e., the sign of surface potential is indeed determined by screening charges rather than by polarization charges.

Thus, observation of thermal phase transition, domain wall motion and PFM imaging indicate that the potential of the surface is inverse to that expected, i.e., polarization charges are completely screened or overscreened. Since no charge deposition is expected during the noncontact measurements and overscreening is unlikely in the pristine state, complete screening occurs on $BaTiO_3$(100) surface in air. The contribution of free charge to the observed potential features must be very small, a conclusion that is further corroborated by force gradient-distance and force-distance analysis.

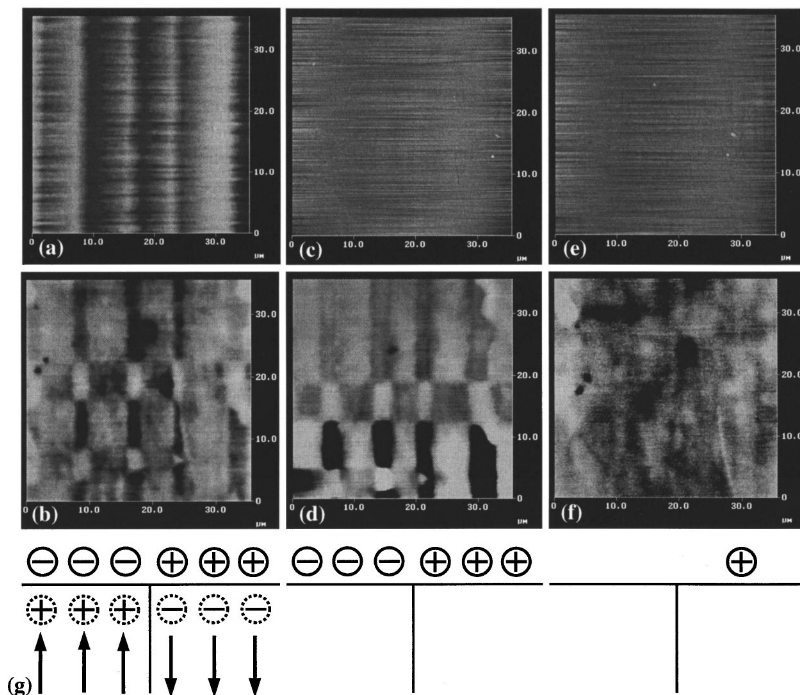

FIG. 6. Surface topography and potential distribution at $BaTiO_3$ (100) surface before ferroelectric phase transition at 125 °C (a), (b), 4 min after transition (c), (d) and after 2.5 h annealing at 140 °C (e), (f). Apparent intensity differs due to the different scale [0.1 V for (b), 0.5 V for (d) and 0.05 V for (f)]. Note that the sign of surface potential features does not change during the transition. Diagram of charge behavior during the phase transition (g). Above T_c, the spontaneous polarization disappears as indicated by the absence of topographical corrugations. Screening charges are uncompensated resulting in the *increase* of domain contrast. Slow relaxation of screening charges results in disappearance of contrast after annealing.

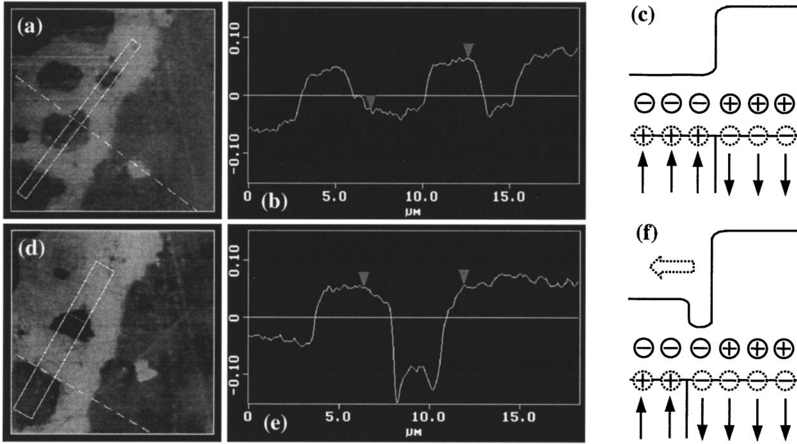

FIG. 7. Surface potential images of c^{+}-c^{-} domain region $BaTiO_3$ (100) acquired at 12 h interval (a), (d), corresponding average profiles along the boxes (b), (e) and the scheme of surface charge distribution (c), (f). Formation of the negative rim in the direction of the domain wall motion is due to the slow relaxation of the screening charges.

C. Bias and height dependence of force gradient

The bias dependence of the average force gradient and the domain force gradient are compared in Fig. 9. As expected, the average force gradient is a parabolic function of the bias voltage; the experimental data are described by Eq. (11). The zeroth-order term $A_0 \approx 60\,\mathrm{Hz}$ includes a frequency offset due to drift in the oscillating characteristics of the cantilever after calibration and depends on the tip. The domain force gradient dependence is linear and is approximated by Eq. (13). Large biases result in nonlinear behavior of the domain force gradient even though the average force gradient follows Eq. (11) well. In order to minimize the influence of this effect, fitting was performed within the linear region. The distance dependence for the average force gradient and domain force gradient is shown in Fig. 10 for several tip biases along with corresponding fits by Eq. (6b). It is clearly seen that a nonlinear response in domain force gradient exists for all tip-surface separation studied.

In order to quantify the distance dependence of EFM data, coefficients A_2 and B_1 for two tips were determined as a function of tip-surface separation (Fig. 11). These dependencies can be linearized in log-log coordinates and corresponding effective slopes are summarized in Table I. The effective slopes are larger than expected for the line charge model (-1) and smaller than expected for the sphere model (-2), in agreement with previous studies on different systems.[64] As expected, the effective slope is smaller for a sharp tip, since the relative contribution of the tip bulk (i.e., line charge contribution) is larger in this case. In fact, the effective slope of the average force gradient for a sharp tip is almost equal to unity, implying that the line charge model can be used to describe the capacitive interaction in this case. To quantify the relative apex and bulk contributions to A_2 and B_1, experimental dependencies were fitted by Eq. (6b) and fitting parameters are listed in Table I.

The frequency shift due to force gradient can be found from Eqs. (1) and (4) as

$$\Delta\omega_{\mathrm{im}} = \frac{\omega_0}{2k}\frac{4\pi\varepsilon_0 V^2}{\beta^2}\frac{1}{h}. \tag{22}$$

Substituting the resonant frequency of the ''dull'' cantilever $\omega_0 = 68.14\,\mathrm{kHz}$, a typical spring constant for the cantilever $k = 1-5\,\mathrm{N/m}$ and a typical tip half-angle $\theta \approx 17°$, the frequency shift according to Eq. (22) yields coefficient c in $\Delta\omega_{\mathrm{im}} = cV^2/h$ equal to 235–47 nm/s V^2, which is in excellent agreement with our experimental results. The spring constant for the tip is therefore estimated as $k \approx 1.75\,\mathrm{N/m}$.

As shown above, the distance dependence of ratios of fitting coefficients can be used to determine the relative contributions of different factors to imaging contrast. The distance dependence of ratios B_1/A_2 and B_0/B_1 for sharp and dull tips are compared in Fig. 12(a). It is clearly seen that for small tip-surface separations ($z < 100\,\mathrm{nm}$) the ratios are almost distance independent. For larger tip-surface separations the measured values of domain force gradient and variations of average force gradient are small compared to typical noise levels (~0.1–1 Hz), consequently errors in fitting coefficients are large in this region. Average potential determined from A_1/A_2 [Eq. (14)] is shown in Fig. 12(b) and summarized in Table II. The absolute potential difference between adjacent domains is calculated as $668\,\mathrm{mV} - 533\,\mathrm{mV} = 135\,\mathrm{mV}$ (dull) and $628\,\mathrm{mV} - 473\,\mathrm{mV} = 155\,\mathrm{mV}$ (sharp). Therefore, the potential difference between c^{+} and c^{-} domains is $\Delta V_{c-c} \approx 135-155\,\mathrm{mV}$. Noteworthy is that the average image potential V_{av} is approximately equal to (V_1

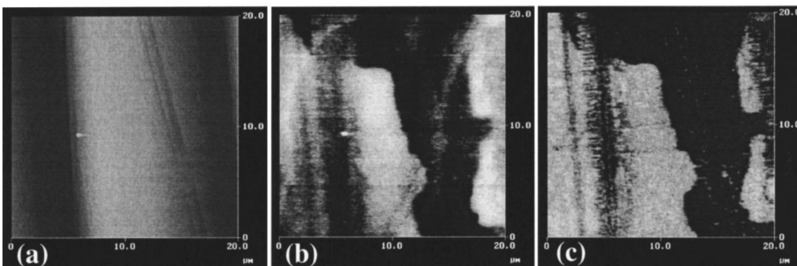

FIG. 8. Surface topography (a), surface potential (b) and piezoresponse images (c) from a-c domain region on $BaTiO_3$ (100) surface.

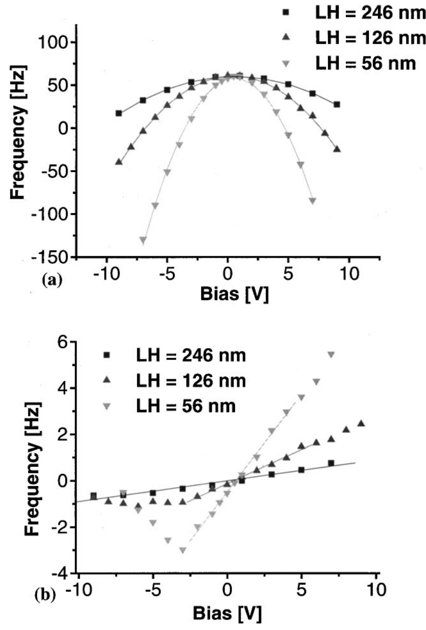

FIG. 9. Bias dependence of average frequency shift (a) and domain frequency shift (b) in force gradient (EFM) images.

$+V_2)/2$, i.e., effective surface areas of c^+ and c^- domain regions are equal, as expected from energy considerations. The potential difference between a and c^+ domains was similarly found to be 85 mV, i.e., approximately equal to the expected value $\Delta V_{a-c} \approx \Delta V_{c-c}/2$. Domain potentials V_1 and V_2, and average image potential V_{av} are combinations of four independent parameters A_1, A_2, B_0 and B_1 and thus are independent.

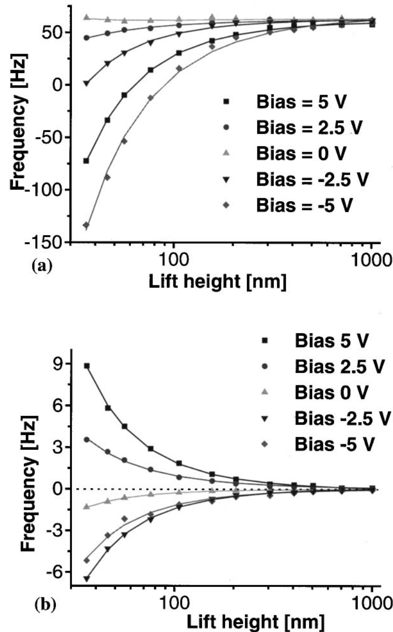

FIG. 10. Distance dependence of average frequency shift (a) and domain frequency shift (b) in force gradient (EFM) images for different tip biases.

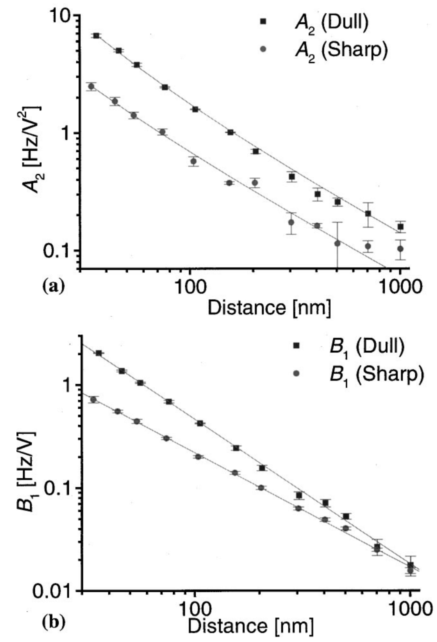

FIG. 11. Coefficients A_2 (a) and B_1 (b) as a function of tip-surface separation for blunt and sharp tip.

D. Bias and height dependence of surface potential

In contrast to EFM that directly measures force gradient, SSPM provides information about forces acting on the tip. Despite superior resolution and better stability of SSPM compared to EFM, the interpretation of contrast formation is complex. Specifically, the measured potential depends on the driving voltage and tip-surface distance so an understanding of image contrast is required to quantify SSPM data.

Quantification of the SSPM data was done similar to the EFM data, i.e., average image potential and potential difference across the domain boundary were determined. Both driving voltage and tip-surface separation dependencies were measured. According to Eq. (3), surface potential measured by SSPM is independent of bias voltage. In practice, however, the nonideality of the feedback loop results in $1/V_{\mathrm{ac}}$ dependence on driving amplitude, as shown in Eq. (18). Thus, the average image potential V_{av} is fit by $V_{\mathrm{av}} = V_s + B/V_{\mathrm{ac}}$, where V_s is surface potential and B is fitting parameter (Fig. 13). Average surface potential is virtually distance independent, $V_s = 600 \pm 20$ mV and coincides with the average surface potential determined by EFM. The coefficient B increases for large tip-surface separations as predicted by Eq. (18).

TABLE I. Distance dependence of average (A) and domain (D) frequency shifts.

Tip	Effective slope	γ, N nm^2/V^2	η, N nm/V^2
Dull A	-1.17 ± 0.04	4000 ± 300	136 ± 7
Sharp A	-1.02 ± 0.05	860 ± 150	60 ± 4
Dull D	-1.41 ± 0.02	1600 ± 70	28 ± 1.5
Sharp D	-1.11 ± 0.01	144 ± 23	20.5 ± 0.6

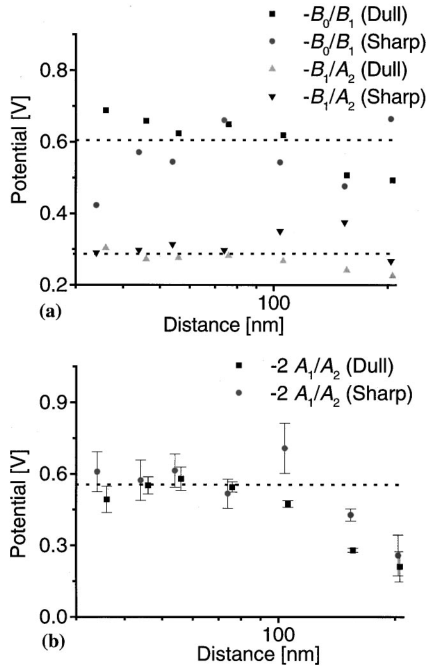

FIG. 12. Distance dependence of universal fitting coefficient ratios B_0/B_1 and B_1/A_2 (a) and $-2A_1/A_2$ (b) for sharp and dull tips. Note that the ratios are independent on distance, while the coefficient *per se* decreases by more than an order of magnitude.

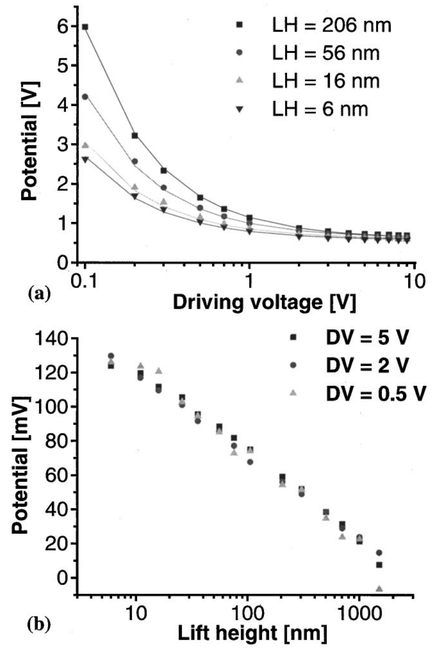

FIG. 13. Driving voltage dependence of average image potential (a) and distance dependence of domain potential difference (b).

The domain potential difference ΔV_{dc} is virtually V_{ac} independent above 2 V, in agreement with Eq. (20). At low driving voltages there is considerable noise and possibly a small increase in measured potential. However, this effect does not exceed ~10–20 mV, while the dependence of the average image potential [see Fig. 13(a)] indicates a strong driving voltage dependence. This observation implies that domain boundary potential differences obtained by SSPM are relatively insensitive to feedback parameters and Eq. (16) can be used to describe potential-distance relations. This also demonstrates that feedback parameters that strongly influence the absolute value of measured surface potential do not affect measured potential variations. The domain potential-distance dependence is shown in Fig. 13(b). In agreement with previous discussion, these values are almost independent of driving voltage, and in fact are almost linear in semilogarithmic coordinates in good agreement with Eq. (18). The distance dependence of domain potential differences were fitted by $y=a+b\ln(x)$. From Eq. (18) the ratio $a/b=\ln(L/4)$ and yield the effective tip length as $L\approx 14\ \mu$m for all tips used, i.e., very close to expected tip length ($L=10$–$15\ \mu$m). The distance dependence of domain potential difference does not saturate in the tip-surface separation range studied, i.e., SSPM does not determine ''true'' potential difference between the domains because of the significant cantilever contribution to the measurements. Imaging at even smaller tip-surface separations suffers from imaging instabilities and the possibility for tip-induced polarization switching and charge transfer.

E. Screening mechanism

Both EFM and SSPM contrast is found to be uniform within the domains with rapid variation at the domain boundaries. Potential and force gradient features are virtually domain-size independent. From these considerations, the origin of the contrast can be attributed either to pure electrostatic field contrast for an unscreened surface [Fig. 2(b)] or surface potential contrast on a completely screened surface [Fig. 2(c)]. Both EFM and SSPM yield potential difference between c^+ and c^- domains as $\Delta V_{c-c}\approx 150$ mV and between a and c domains as $\Delta V_{a-c}\approx\Delta V_{c-c}/2$. This value is much smaller than that expected for an unscreened surface. Furthermore, observations of the ferroelectric phase transition and domain wall motion suggest that the potential of surface domains is inverse to that expected from polarization orientation, i.e., it is negative for c^+ domains and positive for c^- domains. This is further verified by the distance dependence of the universal coefficient ratios (Fig. 12). There-

TABLE II. Fitting coefficient ratios for EFM imaging of ferroelectric domains.

Tip	$2(V_1-V_2)=-B_1/A_2$	$(V_1+V_2)/2=-B_0/B_1$	$V_{av}=-A_1/2A_2$
Dull	0.27±0.03	0.60±0.08	0.53±0.05
Sharp *c-c*	0.31±0.04	0.55±0.09	0.60±0.07
Sharp *a-c*	0.17±0.02	0.63±0.09	0.60±0.07

fore, the state of the ferroelectric $BaTiO_3$ (100) surface under ambient conditions corresponds to almost complete screening of polarization bound charges.

While complete screening and overscreening are expected when domain switching is induced by a charged tip, the pristine equilibrium domain structure is studied here. The sign of the potential features indicates that screening charges are located closer to the tip than potential bound charges. This consideration is not sufficient to attribute the screening to surface adsorbates, since analysis of the ferroelectric screening problem indicates that the electrostatic field can be parallel to polarization in the surface layer (while it is always depolarizing in the bulk) giving rise to the same sign rule. Equation (A7) suggests that a potential difference of 0.175 V is equivalent to a 0.25 nm double layer of a dielectric constant $\varepsilon_1=80$ (H_2O) on a ferroelectric substrate (external screening) or a 9.5 nm depletion layer in a ferroelectric with a dielectric constant $\varepsilon_2=3000$ (intrinsic screening). While the former estimate is reasonable for a molecular adsorbate layer or occupation/depletion of surface states, the latter is unreasonably small for a depletion layer width in a semiconductor with a low charge carrier concentration ($\sim 1\ \mu$m). Thus, surface adsorption or intrinsic surface states are the dominant mechanism for polarization screening on a ferroelectric surface in ambient conditions, though a minor contribution from intrinsic screening cannot be excluded. Noteworthy is that the average surface potential is approximately equal to average domain potential between c^+ and c^- domains, $V_{av}\approx(V_1+V_2)/2$. This observation implies that surface areas occupied by c^+ and c^- domains are equal, as expected from considerations of electrostatic energy minimization.

V. CONCLUSIONS

The combination of AFM, EFM and SSPM provides a powerful tool to determine surface and subsurface domain structures on well-defined $BaTiO_3$ (100) surfaces. EFM and SSPM analyses of domain wall motion and thermal phase transition indicate that polarization bound charge is completely screened on this surface and surface potential is reverse to that expected from domain polarity. These conclusions are corroborated by piezoresponse force microscopy. Analytical treatment of force gradient-distance (EFM) and force-distance (SSPM) data requires both cantilever and tip contributions to be taken into account. Quantification of EFM data allows extraction of absolute domain potentials with respect to the tip. Extracted potential differences between domains of opposite polarities suggest that polarization bound charge is completely screened by adsorbates, charge carriers, or intrinsic surface states. Surface potential from SSPM data does not saturate for small tip-surface separations and consequently special precautions should be taken in quantifying these data. Measured potential variations are also found to be independent of feedback parameters unlike the absolute values of surface potential.

ACKNOWLEDGMENTS

We acknowledge the support from MRSEC Grant No. NSF DMR 00-79909. The authors are grateful to D. L. Gorbachev for the development of image analysis software and A. Farrow for SEM measurements.

APPENDIX: POTENTIAL AND FIELD ABOVE FERROELECTRIC SURFACE

The surface layer in a ferroelectric material with an arbitrary degree of polarization screening with periodic c^+-c^- domain structure in x direction can be approximated by sheets of charge $\sigma^+(-L/2<x<L/2)$ and $-\sigma^+(L/2<x<3L/2)$ at $z=0$ and $\sigma^-(-L/2<x<L/2)$ and $-\sigma^-(L/2<x<3L/2)$ at $z=-h$, where L is characteristic domain size and h is characteristic width of double layer. The dielectric constant is ε_0 for $z>0$ above ferroelectric surface, ε_1 for $-h<z<0$ in the double layer, and ε_2 for $z<-h$. For a completely screened surface $\sigma^+=-\sigma^-=\sigma$, while for the unscreened surface $\sigma^-=0$. For internal screening by charge carriers $\varepsilon_1\approx\varepsilon_2\approx 3000\varepsilon_0$, corresponding to pure $BaTiO_3$, while for external screening by adsorbates $\varepsilon_2\approx 80\varepsilon_0$ (as for H_2O). For a tetragonal ferroelectric ε_2 is determined as a geometric mean of principal values of dielectric constant tensor $\varepsilon_2=\sqrt{\varepsilon_x\varepsilon_z}$.

The potential above the surface, in the double layer and in the bulk can be written as a Fourier series:

$$\Phi_1=\sum_{n=0} A_n \cos\left(\frac{\pi n x}{L}\right)\exp\left(-\frac{\pi n y}{L}\right), \quad z>0, \quad \text{(A1)}$$

$$\Phi_1=\sum_{n=0}\left[B_n\exp\left(-\frac{\pi n y}{L}\right)+C_n\exp\left(\frac{\pi n y}{L}\right)\right]\cos\left(\frac{\pi n x}{L}\right),$$
$$-h<z<0, \quad \text{(A2)}$$

$$\Phi_1=\sum_{n=0} D_n \cos\left(\frac{\pi n x}{L}\right)\exp\left(\frac{\pi n y}{L}\right), \quad z<-h. \quad \text{(A3)}$$

The coefficients A_n, B_n, C_n, D_n are determined from the usual boundary conditions for potential:

$$\Phi_1(z=0)=\Phi_2(z=0), \quad \text{(A4a)}$$

$$\Phi_2(z=-h)=\Phi_3(z=-h) \quad \text{(A4b)}$$

and electric field

$$\varepsilon_0\frac{\partial\Phi_1(z=0)}{\partial z}-\varepsilon_1\frac{\partial\Phi_2(z=0)}{\partial z}=\sigma^+, \quad \text{(A5a)}$$

$$\varepsilon_1\frac{\partial\Phi_2(z=-h)}{\partial z}-\varepsilon_2\frac{\partial\Phi_3(z=-h)}{\partial z}=\sigma^-. \quad \text{(A5b)}$$

The potential and field distribution above a ferroelectric surface is determined by the coefficient A_n. Its functional form is complicated, but since the width of double layer is much smaller than the characteristic domain size, $h\ll L$, A_n can be calculated as

$$A_n = \frac{4h\sigma\varepsilon_2}{\varepsilon_1(1+\varepsilon_2)} \frac{(-1)^{n+1}}{\pi(1+2n)}. \tag{A6}$$

From Eq. (A1), (A6) potential difference between the c^+ and c^- domains in the completely screened case is

$$\Delta V^s = \Phi_1(L,0) - \Phi_1(0,0) = \frac{h\sigma\varepsilon_2}{\varepsilon_0\varepsilon_1(1+\varepsilon_2)}, \tag{A7}$$

while the field variation is

$$\Delta E^s = E_1(L,0) - E_1(0,0) = \frac{2h\sigma\varepsilon_2}{\varepsilon_0\varepsilon_1(1+\varepsilon_2)L}. \tag{A8}$$

In the unscreened case the potential and electric field difference between c^+ and c^- domains is

$$\Delta V^u = \Phi_1(L,0) - \Phi_1(0,0) = \frac{4CL\sigma}{\varepsilon_0(1+\varepsilon_2)\pi^2}, \tag{A9}$$

where $C \approx 0.916$ is the Catalan constant and

$$\Delta E^u = E_1(L,0) - E_1(0,0) = \frac{\sigma}{\varepsilon_0(1+\varepsilon_2)}. \tag{A10}$$

*Email: bonnell@sol1.lsrm.upenn.edu

[1] A. Beck, J. G. Bednorz, Ch. Gerber, C. Rossel, and D. Widmer, Appl. Phys. Lett. **77**, 139 (2000).
[2] D. L. Polla and L. F. Francis, Annu. Rev. Mater. Sci. **28**, 563 (1998).
[3] M. E. Lines and A. M. Glass, *Principles and Applications of Ferroelectric and Related Materials* (Clarendon, Oxford, 1977).
[4] *Ferroelectric Ceramics*, edited by N. Setter and E. L. Colla (Birkhauser-Verlag, Basel, 1993).
[5] B. Jaffe, W. R. Cook, Jr., and H. Jaffe, *Piezoelectric Ceramics* (Academic, New York, 1971).
[6] *Ceramic Materials for Electronics*, edited by R. Buchanan (Marcel Dekker, New York, 1991).
[7] *Electronic Ceramics: Properties, Devices and Applications*, edited by L. M. Levinson (Marcel Dekker, New York, 1988).
[8] V. P. Dudkevich, I. N. Zakharchenko, and E. G. Fesenko, Ferroelectrics **18**, 185 (1978).
[9] U. T. Hoechli and D. W. Pohl, Ferroelectrics **13**, 403 (1976).
[10] Z. Surowiak, P. Wawrzala, and V. P. Dudkevich, Surf. Rev. Lett. **5**, 409 (1998).
[11] V. Z. Borodin and E. Y. Schneider, Ferroelectrics **13**, 407 (1976).
[12] I. I. Ivanchik, Ferroelectrics **145**, 149 (1993).
[13] Y. G. Wang, J. Dec, and W. Kleemann, J. Appl. Phys. **84**, 6795 (1998).
[14] A. L. Gruverman, J. Hatano, and H. Tokumoto, Jpn. J. Appl. Phys. **36**, 2207 (1997).
[15] M. Takashige, S.-I. Hamazaki, N. Fukurai, F. Shimizu, and S. Kojima, Jpn. J. Appl. Phys. **35**, 5181 (1996).
[16] M. Takashige, S.-I. Hamazaki, F. Shimizu, and S. Kojima, Ferroelectrics **196**, 211 (1997).
[17] S. Balakumar, J. B. Xu, J. X. Ma, S. Ganesamoorthy, and I. H. Wilson, Jpn. J. Appl. Phys. **36**, 5566 (1997).
[18] G. K. H. Pang and K. Z. Baba-Kishi, J. Phys. D **31**, 2846 (1998).
[19] L. M. Eng, M. Friedrich, J. Fousek, and P. Günter, J. Vac. Sci. Technol. B **14**, 1191 (1996).
[20] H. Bluhm, U. D. Schwartz, and R. Wiesendanger, Phys. Rev. B **57**, 161 (1998).
[21] A. Correia, J. Massanell, N. Garcia, A. P. Levanyuk, A. Zlatkin, and J. Przeslawski, Appl. Phys. Lett. **68**, 2796 (1996).
[22] R. Lüthi, H. Haefke, K.-P. Meyer, E. Meyer, L. Howald, and H.-J. Güntherodt, J. Appl. Phys. **74**, 7461 (1993).
[23] R. Lüthi, H. Haefke, W. Gutmannsbauer, E. Meyer, L. Howald, and H.-J. Güntherodt, J. Vac. Sci. Technol. B **12**, 2451 (1996).
[24] B. D. Terris, J. E. Stern, D. Rugar, and H. J. Mamin, Phys. Rev. Lett. **63**, 2669 (1989).
[25] J. Ohgami, Y. Sugawara, S. Morita, E. Nakamura, and T. Ozaki, Jpn. J. Appl. Phys. **35**, 2734 (1996).
[26] L. M. Eng, J. Fousek, and P. Günter, Ferroelectrics **191**, 211 (1997).
[27] P. Lehnen, J. Dec, and W. Kleemann, J. Phys. D **33**, 1932 (2000).
[28] A. Gruverman, O. Auciello, and H. Tokumoto, J. Vac. Sci. Technol. B **14**, 602 (1996).
[29] O. Kolosov, A. Gruverman, J. Hatano, K. Takahashi, and H. Tokumoto, Phys. Rev. Lett. **74**, 4309 (1995).
[30] A. Gruverman, O. Auciello, and H. Tokumoto, Annu. Rev. Mater. Sci. **28**, 101 (1998).
[31] G. Zavala, J. H. Fendler, and S. Trolier-McKinstry, J. Appl. Phys. **81**, 7480 (1997).
[32] L. M. Eng, H.-J. Güntherodt, G. A. Schneider, U. Kopke, and J. Muñoz Saldaña, Appl. Phys. Lett. **74**, 233 (1999).
[33] S. V. Kalinin and D. A. Bonnell, Phys. Rev. B **62**, 10419 (2000).
[34] D. Sarid, *Scanning Force Microscopy* (Oxford University Press, New York, 1991).
[35] C. Durkan, M. E. Welland, D. P. Chu, and P. Migliorato, Phys. Rev. B **60**, 16198 (1999).
[36] H. J. Ding, P. F. Hou, and F. L. Guo, Int. J. Solids Struct. **37**, 3201 (2000).
[37] V. Z. Parton and B. A. Kudryavtsev, *Electromagnetoelasticity* (Gordon and Breach, New York, 1988).
[38] A. E. Giannakopoulos and S. Suresh, Acta Mater. **47**, 2153 (1999).
[39] S. A. Melkumyan and A. F. Ulitko, Prikl. Mat. Mekh. **23**, 44 (1987).
[40] E. Karapetian, I. Sevostianov, and M. Kachanov, Philos. Mag. B **80**, 331 (2000).
[41] A. Gruverman, Appl. Phys. Lett. **75**, 1452 (1999).
[42] C. S. Ganpule, V. Nagarjan, H. Li, A. S. Ogale, D. E. Steinhauer, S. Aggarwal, E. Williams, R. Ramesh, and P. DeWolf, Appl. Phys. Lett. **77**, 292 (2000).
[43] C. Durkan, D. P. Chu, P. Migliorato, and M. E. Welland, Appl. Phys. Lett. **76**, 366 (2000).
[44] K. Lee, H. Shin, W. K. Moon, J. U. Jeon, and Y. E. Park, Jpn. J. Appl. Phys. **38**, L264 (1999).
[45] K. Franke, H. Huelz, and M. Weihnacht, Surf. Sci. **415**, 178 (1998).
[46] L. M. Eng, H. J. Güntherodt, G. Rosenman, A. Skliar, M. Oron, M. Katz, and D. Eger, J. Appl. Phys. **83**, 5973 (1998).

[47] G. Mesa, E. Dobado-Fuentes, and J. J. Saenz, J. Appl. Phys. **79**, 39 (1996).
[48] H. W. Hao, A. M. Baro, and J. J. Saenz, J. Vac. Sci. Technol. B **9**, 1323 (1991).
[49] S. Belaidi, P. Girard, and G. Leveque, J. Appl. Phys. **81**, 1023 (1997).
[50] F. Saurenbach and B. D. Terris, Appl. Phys. Lett. **56**, 1703 (1990).
[51] J. W. Hong, K. H. Noh, S. I. Park, S. I. Kwun, and Z. G. Kim, Rev. Sci. Instrum. **70**, 1735 (1999).
[52] E. Z. Luo, Z. Xie, J. B. Xu, I. H. Wilson, and L. H. Zhao, Phys. Rev. B **61**, 203 (2000).
[53] V. M. Fridkin, *Ferroelectric Semiconductors* (Consultants Bureau, New York, 1980).
[54] E. V. Chenskii, Fiz. Tverd. Tela (Leningrad) **12**, 586 (1970).
[55] X. Q. Chen, H. Yamada, T. Horiuchi, K. Matsushige, S. Watanabe, M. Kawai, and P. S. Weiss, J. Vac. Sci. Technol. B **17**, 1930 (1999).
[56] T. Tybell, C. H. Ahn, L. Antognazza, and J.-M. Triscone, Vide: Sci., Tech. Appl. **289**, 551 (1998).
[57] A. Efimov and S. R. Cohen, J. Vac. Sci. Technol. A **18**, 1051 (2000).
[58] *Command Reference Manual* (Digital Instruments, Santa Barabara, 1997).
[59] Y. Cho, S. Kazuta, and K. Matsuura, Appl. Phys. Lett. **75**, 2833 (1999).
[60] S. V. Kalinin and D. A. Bonnell, Appl. Phys. Lett. **78**, 1116 (2001).
[61] S. V. Kalinin and D. A. Bonnell, J. Appl. Phys. **87**, 3950 (2000).
[62] S. V. Kalinin and D. A. Bonnell, Z. Metallkd. **90**, 983 (1999).
[63] S. V. Kalinin, C. Y. Johnson, and D. A. Bonnell, Phys. Rev. B (to be published).
[64] Y. Liang, D. A. Bonnell, W. D. Goodhue, D. D. Rathman, and C. O. Bozler, Appl. Phys. Lett. **66**, 1147 (1995).